

Research



Cite this article: Nitschke I, Reuther S, Voigt A. 2020 Liquid crystals on deformable surfaces. *Proc. R. Soc. A* **476**: 20200313.
<http://dx.doi.org/10.1098/rspa.2020.0313>

Received: 23 April 2020

Accepted: 17 July 2020

Subject Areas:

materials science, mathematical modelling, biophysics

Keywords:

nematic liquid crystal, shape relaxation, gradient flow

Author for correspondence:

Axel Voigt

e-mail: axel.Voigt@tu-dresden.de

Electronic supplementary material is available online at <https://doi.org/10.6084/m9.figshare.c.5107141>.

Liquid crystals on deformable surfaces

Ingo Nitschke¹, Sebastian Reuther¹ and Axel Voigt^{1,2,3}

¹Institute of Scientific Computing, TU Dresden, 01062 Dresden, Germany

²Center for Systems Biology Dresden (CSBD), Pfortenhauerstraße 108, 01307 Dresden, Germany

³Cluster of Excellence Physics of Life (PoL), 01062 Dresden, Germany

AV, 0000-0003-2564-3697

Liquid crystals with molecules constrained to the tangent bundle of a curved surface show interesting phenomena resulting from the tight coupling of the elastic and bulk-free energies of the liquid crystal with geometric properties of the surface. We derive a thermodynamically consistent Landau-de Gennes-Helfrich model which considers the simultaneous relaxation of the Q -tensor field and the surface. The resulting system of tensor-valued surface partial differential equation and geometric evolution laws is numerically solved to tackle the rich dynamics of this system and to compute the resulting equilibrium shape. The results strongly depend on the intrinsic and extrinsic curvature contributions and lead to unexpected asymmetric shapes.

1. Introduction

In-plane order on two-dimensional manifolds has been the subject of much research elucidating the intimate relation between topological defects and the geometry of the manifold. Depending on the topology of the manifold these defects can not only be energetically favourable, but topologically necessary. They can play fundamental roles leading to striking results and structures in the ground state that would be highly suppressed in flat systems. Such properties are summarized in [1,2] for positional and orientational order, respectively. Colloidal crystals assembled on spherical or toroidal surfaces provide good examples to study the role of curvature on positional ordering. Here, the number of defects can deviate from the minimal topologically required defect set, leading to scars and pleats in the ground state, e.g. [3,4].

Orientational ordering has been analysed in the context of liquid crystals. Due to the close relation between principle curvature and Q -tensor field the coupling between geometric properties and defects becomes even tighter, leading to e.g. non-required defects on a torus [5]. On a sphere the ground state has been identified as a tetrahedral configuration [6] and coated spherical colloids with functionalized defects have been proposed as building blocks for colloidal crystals with a tetrahedral structure [7].

In contrast to these studies on fixed surfaces, we allow the manifold to change. This additional relaxation mechanism provides a path to locally overcome geometric frustration. The tendency to accommodate some preferential in-plane order is the mechanism behind the buckling of crystalline sheets [8] and also the origin of the icosahedral shape of various viral capsids [9]. While the interplay of crystalline order and shape relaxation has been studied theoretically and computationally, e.g. [8–10], the situation for nematic order is less explored. Defects in nematic shells are intensively studied on fixed geometries, such as a sphere [6,11–14] and under more complicated constraints, e.g. [15–19]. Most of these studies use particle methods. However, field theoretical descriptions also exist, e.g. [20–25]. These models differ in details and strongly depend on the assumptions made in the derivation. While most of them only focus on the steady state, some also account for dynamics via gradient flows, e.g. [24,25]. These approaches are well suited to be extended towards changing manifolds. An attempt in this direction can be found in [26] for polar order, where the model in [24] is generalized to manifolds with a prescribed evolution. We are interested in the resulting equilibrium shapes if both the manifold and the orientational order on it are allowed to relax. Analytical results within a simplified phenomenological mean-field theory [27] suggest shape changes from spherical to tetrahedral. We will show that the situation can become more complex if not only intrinsic but also extrinsic curvature contributions are considered. At least for weak bending forces extrinsic curvature contributions can break the symmetry, making the tetrahedral defect configuration unstable. The change from a tetrahedral to a planar defect arrangement has strong implications for the aforementioned applications. Such shape changes are also relevant in the understanding of morphological changes during development and the design of bioinspired materials that are capable of self-organization. Defect dynamics and corresponding morphological transitions have been observed by restricting suspensions of microtubule filaments driven by kinesin motors to the membrane of vesicles [28]. The observed shape changes are tunable and lead to ring-shaped, spindle-shaped and motile droplets with filipodia-like protrusions. To fully understand these complex out-of-equilibrium systems, first an understanding of systems without active components is necessary. We will, therefore, only focus on passive systems and leave the investigation of additional active terms for future research.

The outline of the paper is as follows: we start in §2 with the derivation of thermodynamically consistent models resulting from an Landau-de Gennes-Helfrich energy. Section 3 describes the numerical approach to solve the resulting geometric and tensor-valued surface partial differential equations. The equations are solved in §4 for specialized situations with increasing complexity, including the evolution of the Q -tensor field on surfaces with a prescribed normal velocity, the surface response to a stationary Q -tensor field and the fully coupled system. We further discuss the results and explain the observed phenomena as a result of the tight coupling of intrinsic and extrinsic curvature with the Q -tensor field and the corresponding topological defects. All modelling and numerical details are provided in the appendix.

2. Notation and model derivation

To obtain the desired equilibrium shapes, we derive steepest decent models for the Landau-de Gennes-Helfrich energy $\hat{U}^Q = \hat{U}^Q(S, q)$, which is specified below. Thereby, $q \in \mathcal{QS}$ is a tangential surface Q tensor, with $\mathcal{QS} = \{\mathbf{r} \in T^2S : \text{Tr } \mathbf{r} = 0, \mathbf{r} = \mathbf{r}^T\}$. Furthermore, $S = S(t)$ is a time-dependent surface without boundary, which evolves only in the normal direction, and $T^n S$ denotes the tangential tensor bundle of degree $n \geq 0$.

We will consider variations of the energy $\hat{\mathcal{U}}^Q$. This requires to identify dependencies and to provide ways how to handle them. The restriction to normal deformations allows to describe the surface by an independent scalar-valued variable $\xi = \xi(t) \in T^0S$. We deploy the ansatz $X = X(\xi) = X(\xi(t, y^1, y^2), y^1, y^2)$ for a time-dependent parametrization to locally describe the surface S . We thus obtain

$$\dot{X} := \frac{d}{dt}X = \frac{\partial \xi}{\partial t} \frac{\partial X}{\partial \xi} = v \mathbf{v}, \quad (2.1)$$

with normal velocity $v = \partial \xi / \partial t$ and normal vector $\mathbf{v} = \partial X / \partial \xi$. Moreover, a perturbation of the surface gives a scalar-valued perturbation in the normal direction by $\delta \xi$, i. e.

$$\delta X = \frac{\partial X}{\partial \xi} \delta \xi = \delta \xi \mathbf{v}. \quad (2.2)$$

Considering the perturbed surface \tilde{S} locally defined by $\tilde{X} = X + \varepsilon \delta X$, we introduce the surface derivative $\delta_S := d/d\varepsilon|_{\varepsilon=0}$ for all quantities of S , which are extendable to \tilde{S} and are sufficiently smooth. Note that this derivative is consistent w. r. t. the perturbation $\tilde{\xi} = \xi + \varepsilon \delta \xi$ in the sense that for functions $(\hat{f} \circ X)(\xi) = f(\xi)$ holds $\delta_S \hat{f} = \delta_S f$, since $\nabla_{\mathbf{v}} \hat{f} = (d/d\xi) \hat{f} = \partial f / \partial \xi$. Especially, for functionals $\hat{F} = \hat{F}[X]$ and $F = F[\xi] = (\hat{F} \circ X)[\xi]$ the derivative δ_S implies the functional derivative $\delta F / \delta \xi$ w. r. t. ξ , i. e.

$$\delta_S \hat{F} = \delta_S F = \lim_{\varepsilon \rightarrow 0} \frac{F[\xi] - F[\xi + \varepsilon \delta \xi]}{\varepsilon} = \int_S \frac{\delta F}{\delta \xi} \delta \xi \mu = \left(\frac{\delta F}{\delta \xi} \right)^* [\delta \xi], \quad (2.3)$$

see appendix D. Obviously, the surface derivative δ_S is not a tensor operator on $T^n S$ for $n \geq 1$, but on $T^n \mathbb{R}^3|_S$. Therefore, claiming $\delta_S q = 0$ to set q as an independent variable w. r. t. the surface, would again be overdetermined in $T^2 \mathbb{R}^3|_S$. Thus, we rather require $\Pi_S \delta_S q = \Pi_{QS} \delta_S q = 0$ instead and finally get $\delta_S q^{ij} = [Bq + qB]^{ij} \delta \xi$ for the contravariant components, see equation (B 2). Thereby, Π_{QS} denotes the projection into the space of tangential Q-tensors (see below). For further details, refer to appendix B.

(a) Free energy

The Landau-de Gennes-Helfrich energy $\mathcal{U}^Q = \mathcal{U}^Q[\xi, q] = \hat{\mathcal{U}}^Q[X, q]$ is given by

$$\mathcal{U}^Q[\xi, q] = \mathcal{U}_H[\xi] + \mathcal{U}_{\text{LdG}}[\xi, p] + \mathcal{U}_a[\xi], \quad (2.4)$$

where

$$\mathcal{U}_H = \frac{\alpha}{2} \int_S \mathcal{H}^2 \mu, \quad (2.5)$$

$$\mathcal{U}_{\text{LdG}} = \mathcal{U}_{\text{El}} + \mathcal{U}_B, \quad (2.6)$$

$$\mathcal{U}_{\text{El}} = \frac{L}{2} \int_S \|\nabla_S q\|^2 + \|B\|^2 \text{Tr } q^2 + 2S\mathcal{H}(B, q) + \frac{S^2}{2} \|B\|^2 \mu, \quad (2.7)$$

$$\mathcal{U}_B = \int_S a' \text{Tr } q^2 + c \text{Tr } q^4 + C_1 \mu \quad (2.8)$$

and

$$\mathcal{U}_a = \frac{\omega_a}{2} \left(\frac{A - A_0}{A_0} \right)^2 \quad (2.9)$$

are the Helfrich energy, the Landau-de Gennes energy, the elastic energy, the bulk energy and the surface area penalization energy, respectively, with the bending rigidity α , mean curvature \mathcal{H} , Landau-de Gennes constant L , nematic order parameter S , thermotropic parameters a, b and $c, a' = a + \frac{b}{3}S + \frac{c}{6}S^2$, $C_1 = S^2(\frac{a}{6} - \frac{b}{54}S + \frac{c}{72}S^2)$, surface area penalization parameter ω_a , desired surface area A_0 , actual surface area $A := \int_S \mu$, the covariant surface gradient ∇_S and the 2-form μ [29], which here can also be interpreted as the area element. The Landau-de Gennes-Helfrich energy is the one-constant approximation of the energy obtained in [25] with the parameter choice $L_1 = L$,

$L_2 = L_3 = L_6 = 0$ and eigenvalue $\beta = -\frac{S}{3}$ of the auxiliary proper Q -tensor

$$Q = q + \frac{S}{6} \Pi_S - \frac{S}{3} v \otimes v \in \mathcal{Q}\mathbb{R}^3|_S. \quad (2.10)$$

The energy in [25] results in a thin-film limit of the corresponding energy in \mathbb{R}^3 with appropriate boundary conditions. The thermotropic stationary bulk energy $\mathcal{U}_{\mathbb{B}}|_{\xi} = \mathcal{U}_{\mathbb{B}}|_{\xi}[q] = \mathcal{U}_{\mathbb{B}}|_{\xi}[S]$ only depends on the nematic order parameter and has a minimum at $S = (-b + \sqrt{b^2 - 24ac})/(4c)$.

(b) Steepest decent method

For the Landau-de Gennes-Helfrich energy $\mathcal{U}^Q = \mathcal{U}^Q[\xi, q] = \hat{\mathcal{U}}^Q[X, q]$, we consider the L^2 -gradient flow w. r. t. $\xi \in T^0 S$, $q \in \mathcal{Q}S$ and $\Pi_{\mathcal{Q}S} \delta_S q = 0$, i. e.

$$-\frac{\delta \mathcal{U}^Q}{\delta \xi} = k \dot{\xi} = kv \quad (2.11)$$

and

$$-\frac{\delta \mathcal{U}^Q}{\delta q} = k^q \dot{q} = k^q \Pi_{\mathcal{Q}S} \frac{dq}{dt} = k^q \Pi_S \frac{dq}{dt} = k^q \left(\left\{ \partial_t q^{ij} \right\} - v \cdot (Bq + qB) \right) \quad (2.12)$$

where $k, k^q \geq 0$ denote kinematic constants.

With initial conditions we get the steepest decent method for the Landau-de Gennes-Helfrich energy

$$\begin{aligned} kv = & - \left(\alpha + \frac{L}{2} S^2 \right) \left(\Delta_S \mathcal{H} + \mathcal{H} \left(\frac{\mathcal{H}^2}{2} - 2\mathcal{K} \right) \right) \\ & + \mathcal{H} \left(\left(a' - L \left(\frac{\mathcal{H}^2}{2} - 2\mathcal{K} \right) \right) \text{Tr } q^2 + c \text{Tr } q^4 + C_1 \right) \\ & - 2L \text{div}_S \left(q \nabla_{\mathbb{B}} q - \nabla_{\mathbb{B}} q + q : (\nabla_S q) B + \frac{1}{2} \text{Tr } q^2 \nabla_S \mathcal{H} + S (\nabla_{\mathbb{B}} q + q \nabla_S \mathcal{H}) \right) \\ & - L \left(\left((\nabla_S q)^{T(123)} : \nabla_S q, \Pi_{\mathcal{Q}S} B \right) + S \|B\|^2 \langle B, q \rangle \right) + \frac{\omega_a}{A_0^2} (A - A_0) \mathcal{H} \end{aligned} \quad (2.13)$$

and

$$k^q \dot{q} = L \left(\Delta^{\mathbb{B}} q - S \mathcal{H} \Pi_{\mathcal{Q}S} B \right) - \left(L \|B\|^2 + 2a' + 2c \text{Tr } q^2 \right) q, \quad (2.14)$$

with Gaussian curvature \mathcal{K} , surface divergence div_S , directional derivative ∇ , material time derivative \dot{p} , Laplace-Beltrami operator Δ_S , Bochner Laplacian $\Delta^{\mathbb{B}}$ and orthogonal Q -tensor projection $\Pi_{\mathcal{Q}S} B = B - (\mathcal{H}/2)g$ of the shape operator, see appendix B for details. For the definition of the used operators in the above equations, refer to appendix C and [25]. Interestingly, even without bending rigidity, $\alpha = 0$, surface regularization in terms of Helfrich energy contributions is present.

We observe that

$$\frac{d}{dt} \mathcal{U}^Q = \int_S \left(\frac{\delta \mathcal{U}^Q}{\delta \xi} \right) v + \left\langle \frac{\delta \mathcal{U}^Q}{\delta q}, \dot{q} \right\rangle \mu = - \int_S v^2 + \|\dot{q}\|^2 \mu \leq 0, \quad (2.15)$$

see appendix D. Therefore, the energy \mathcal{U}^Q dissipates as long as the solution and the shape are not stationary.

3. Numerical approach

To numerically solve the system (2.13)–(2.14), we use a semi-implicit Euler time-stepping scheme, an operator-splitting ansatz and the generic finite element approach proposed in [30], which is based on a reformulation of all operators and quantities in Cartesian coordinates and penalization of normal components. The approach is general and not restricted to single

connected manifolds. Applications of the latter approach can be found in e.g. [24,26,31]. All equations are implemented in the adaptive finite-element toolbox AMDiS [32,33]. For better readability, we use the abbreviations

$$\begin{aligned}\tilde{\alpha} &= \alpha + \frac{L}{2} S^2, \\ w_q &= -2L(q\nabla_B q - \nabla_q B q + q : (\nabla_S q)B) + \frac{1}{2} \text{Tr } q^2 \nabla_S \mathcal{H} + S(\nabla_B q + q \nabla_S \mathcal{H}) \\ \beta_q &= \mathcal{H} \left(\left(a' - L \left(\frac{\mathcal{H}^2}{2} - 2\mathcal{K} \right) \right) \text{Tr } q^2 + c \text{Tr } q^4 + C_1 \right) \\ &\quad - L(\langle (\nabla_S q)^{T(123)} : \nabla_S q, \Pi_{QS} B \rangle + S \|B\|^2 \langle B, q \rangle)\end{aligned}$$

in the following derivation.

(a) Time discretization

Let $0 = t^0 < t^1 < t^2 < \dots$ be a partition of the time with time-step width $\tau^m := t^m - t^{m-1}$. Each variable/quantity with a superscript index m corresponds to the respective variable/quantity at time t^m . The overall operator-splitting algorithm for the system (2.13)–(2.14) reads as follows: for $m = 1, 2, \dots$ do

- (i) Move geometry according to equation (2.1), i. e. in the time-discrete setting

$$X^m = X^{m-1} + \tau^m v^{m-1} \nu^{m-1}, \quad (3.1)$$

with the parametrization of the initial geometry X^0 and corresponding initial normal vector ν^0 .

- (ii) Update normal vector according to $\partial_t \nu = -\nabla_S \nu$, see equation (D7). Thus, in the time-discrete setting the normal vector at the new time step t^m is determined by

$$\nu^m = \nu^{m-1} - \tau^m \nabla_S \nu^{m-1}. \quad (3.2)$$

- (iii) Update all other geometric quantities, i. e. the mean curvature \mathcal{H}^m , the Gaussian curvature \mathcal{K}^m , the projection Π_S^m and the shape operator B^m , by using the prior computed normal vector ν^m .
- (iv) Update Q -tensor field q^m according to equation (2.14), which read in the time-discrete setting

$$k^q d_q^m = L \left(\Delta^B q^m - S \mathcal{H} \Pi_{QS}^m B^m \right) - \left(L \|B^m\|^2 + 2a' \right) q^m - 2cf^q(q^m, q^{m-1}), \quad (3.3)$$

respectively. Thereby, $d_q^m := \frac{1}{\tau^m} (\Pi_S^m q^m \Pi_S^m - \Pi_S^m q^{m-1} \Pi_S^m)$ denotes the discrete material time derivative and $f^q(q^m, q^{m-1})$ is a linearization of the term $\text{Tr } (q^m)^2 q^m$, see [24].

- (v) Update normal velocity v^m according to equation (2.13), which reads in the time-discrete setting

$$kv^m = -\tilde{\alpha} \left(\Delta_S \mathcal{H}^m + \mathcal{H}^m \left(\frac{(\mathcal{H}^m)^2}{2} - 2\mathcal{K}^m \right) \right) + \beta_q^m + \text{div}_S w_q^m + \frac{\omega_a}{A_0^2} (A^m - A_0) \mathcal{H}^m. \quad (3.4)$$

(b) Space discretization

The remaining step is to discretize eqns. (3.3) and (3.4) from the above algorithm in space by using either the generic surface finite-element method for tensor-valued surface PDEs proposed in [30] or the surface finite-element method for scalar-valued surface PDEs from [34]. Let $S_h = S_h(t)|_{t=t^m}$ be an interpolation of the surface $S = S(t)|_{t=t^m}$ at time t^m such that $S_h := \bigcup_{T \in \mathcal{T}} T$, where \mathcal{T} denotes a conforming triangulation. Furthermore, the finite-element space is introduced as $\mathcal{V}(S_h) := \{v \in \mathcal{C}^0(S_h) : v|_T \in \mathcal{P}^1(T), \forall v \in \mathcal{T}\}$ with $\mathcal{C}^k(S_h)$ the space of k -times continuously differentiable functions

on S_h and $\mathcal{P}^l(T)$ polynomials of degree l on the triangle $T \in \mathcal{T}$. We use the finite-element space $\mathcal{V}(S_h)$ twice as trial and as test space and additionally introduce the L_2 inner product on S_h , i. e. $(\alpha, \beta) := \int_{S_h} \alpha \beta dS$. Thus, the finite-element approximations of equations (3.3) and (3.4) read: find $q^m \in \mathcal{V}(S_h)^{3 \times 3}$ such that $\forall V \in \mathcal{V}(S_h)^{3 \times 3}$

$$\begin{aligned} (k^q d_q^m, V) = & - (L \nabla_S q^m, \nabla_S V) - \left(L (S \mathcal{H} \Pi_{QS}^m B^m) + (L \|B^m\|^2 + 2a') q^m, V \right) \\ & + \left(\omega_t^q \left(q^m \Pi_S^\perp + \Pi_S^\perp q^m + \Pi_S^\perp q^m \Pi_S^\perp \right) - 2cf^q(q^m, q^{m-1}), V \right), \end{aligned} \quad (3.5)$$

and find $v^m \in \mathcal{V}(S_h)$ such that $\forall \gamma \in \mathcal{V}(S_h)$

$$\begin{aligned} (kv^m, \gamma) = & \left(\tilde{\alpha} \nabla_S \mathcal{H}^m - w_q^m, \nabla_S \gamma \right) - \left(\tilde{\alpha} \mathcal{H}^m \left(\frac{(\mathcal{H}^m)^2}{2} - 2\mathcal{K}^m \right), \gamma \right) \\ & + \left(\beta_q^m + \frac{\omega_a}{A_0^2} (A^m - A_0) \mathcal{H}^m, \gamma \right). \end{aligned} \quad (3.6)$$

Note that we here use the same symbols for the extended Q -tensor field as for the local surface quantity. According to the generic surface finite-element method from [30] a penalty term $(\omega_t^q (q^m \Pi_S^\perp + \Pi_S^\perp q^m + \Pi_S^\perp q^m \Pi_S^\perp), V)$ with $\Pi_S^\perp = \mathbf{v} \mathbf{v}^T$ with penalty parameter ω_t^q is added to equation (3.5) to ensure tangentiality of the Q -tensor field. Equation (3.6) has to be stabilized, which is realized by artificial diffusion following ideas of [35] for surface diffusion. In particular, we add the term $(D(\nabla_S v^{m-1} - \nabla_S v^m), \nabla_S \gamma)$ with the artificial diffusion parameter D to the right-hand sides of equation (3.6). This approach is significantly simpler than other proposed discretization schemes, such as [36–38], but also leads to sufficient accuracy for our purposes. Recently, at least for mean curvature flow, a similar method which relays on the evolution of geometric quantities, has been used and analysed in [39]. For more details, especially for evaluating the local inner products in the L_2 inner products for the extended Q -tensor field, refer to [30].

4. Results

In the following, we consider examples for the model (2.13)–(2.14). To visualize the Q -tensor field q , we consider the principal director of the Q -tensor, i. e. the eigenvector for the eigenvalue with the largest absolute value of the Q -tensor. This director has no direction as it is π symmetric and thus represents the same Q -tensor if rotated by an angle of π in the tangent plane.

Firstly, we prescribe the normal velocity of the surface and determine the response of the Q -tensor due to shape changes. Secondly, by changing the model parameters the response of the surface to a given Q -tensor field is investigated. Thirdly, the full model including the interplay of the liquid crystal dynamics and the surface evolution is considered. Thereby, we consider known examples for fixed surfaces from the literature and let the surface evolve. The resulting stationary shape is analysed in detail and compared with its intrinsic counterpart. All used model and simulation parameters are shown in table 1.

(a) Prescribed normal velocity

Here, we only consider equation (2.14) on a prescribed evolving surface $\mathcal{S}(t)$. We focus on the alignment of the director to minimal curvature lines and the localization of topological defects according to curvature. For detailed discussions on stationary surfaces, refer to [24,25]. We adapt the movement used in [26], where a rotationally symmetric ellipsoidal shape with major axes parameters $a_0 = a_1 = 1$ and $a_2 = 1.25$ is considered as starting geometry. These parameters are now considered to be time-dependent, such that the surface area is preserved over time. During the evolution the ellipsoid collapses to a sphere and deforms back to an ellipsoid with a different orientation. As initial condition we use the close-to-equilibrium solutions obtained on

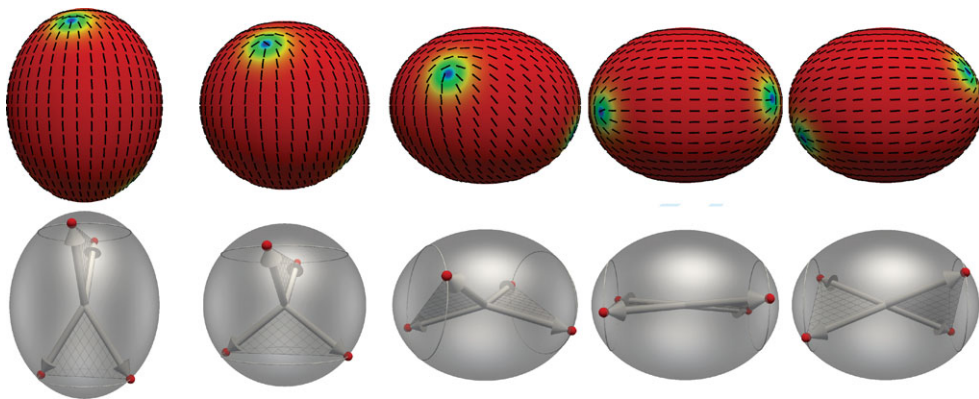


Figure 1. First and second row: Evolution of the Q -tensor field q for $t = 0, 40, 70, 110, 300$ on the prescribed evolving ellipsoid (top row) and respective $+\frac{1}{2}$ defect locations visualized as red dots and grey arrows (bottom row). The defect pairs with the two minimal angles to each other are indicated by the triangular planes. The grey circles indicate rotationally symmetric solutions. The response of the defects to changes in curvature and the alignment along the minimal curvature lines can be observed.

Table 1. Used model and simulation parameters. All values are treated as non-dimensional and can be obtained by, e.g. using the length scale approximately $100 \mu\text{m}$, the time scale approximately 1 s and the energy scale approximately 10^{-17} J , which are typical scales in active liquid crystal systems, e.g. [28,40].

	figures 1–2	figures 3–4	figures 5–6	figures 7–8	figure 9	figure 10
k^q	1	10^8	1	1	—	—
L	0.1966	0.3931	0.3931	0.3931	—	—
a	−6.4862	−13.3333	−13.3333	−13.3333	—	—
b	−4.9138	−10	−10	−10	—	—
c	9.8275	20	20	20	—	—
ω_t^q	10^3	10^3	10^3	10^3	—	—
α	—	0.5	0.5	0.8	1	0.5
k	—	100	100	100	100	100
ω_a	—	500	500	500	500	—
D	—	166.6	166.6	166.6	166.6	166.6
τ_m	0.1	0.0025	0.01	0.001	0.01	0.025

the stationary initial ellipsoid with initial condition

$$q|_{t=0} = S \left((v \times p_q) \otimes (v \times p_q) - \frac{1}{2} \Pi_S \right),$$

$$p_q = \frac{1}{\|\Pi_S \tilde{p}_q\|} \Pi_S \tilde{p}_q, \quad \tilde{p}_q = \begin{cases} (1, 4, 0)^T & , z \geq 0 \\ (-4, 1, 0)^T & , z < 0 \end{cases}$$

for $X = (x, y, z)^T \in S$.

Figure 1 shows the results which clearly indicate the alignment of the director field to the minimal curvature lines. To be more precise, in the beginning, the directors are aligned in a north-south symmetry. After passing the sphere geometry an ellipsoid with different orientation evolves and the directors start to rearrange to be aligned in an east-west symmetry, as expected.

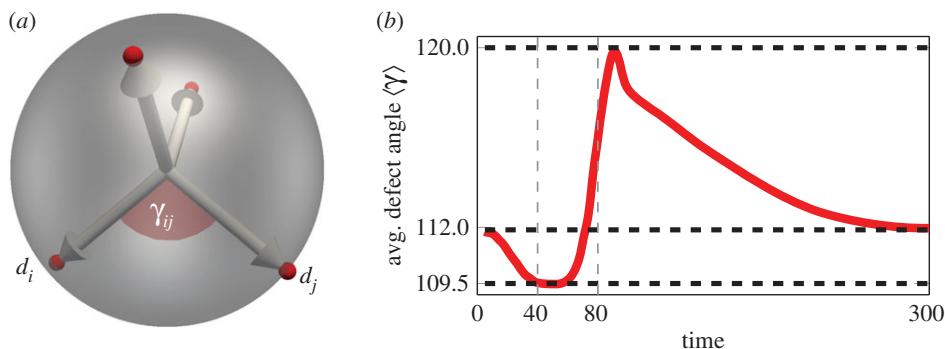


Figure 2. Schematic drawing for defect angles γ_{ij} between defect positions \mathbf{d}_i and \mathbf{d}_j (a) and averaged defect angle $\langle \gamma \rangle = \frac{1}{6} \sum_{i < j} \arccos(\langle \frac{\mathbf{d}_i}{\|\mathbf{d}_i\|}, \frac{\mathbf{d}_j}{\|\mathbf{d}_j\|} \rangle)$ against time for the Landau-de Gennes-Helfrich model (b). 112° is the equilibrium average for the considered ellipsoid at the initial and final configuration, 109.5° and 120° correspond to the tetrahedral and planar defect configuration on a sphere. The surface evolution passes the sphere configuration at $t = 40$ and the final ellipsoidal shape is already reached at $t = 80$ (marked as vertical dashed lines). (Online version in colour.)

Concerning the defects, shown in figure 1 as regions of disturbed orientational order (first row) and highlighted as red dots and grey arrows (second row). For the Landau-de Gennes-Helfrich model, the tetrahedral configuration with four $+\frac{1}{2}$ defects is found. On a sphere, it is known as a global minimizer, subject to rotation [6]. On an ellipsoid the four $+\frac{1}{2}$ defects, even if geometrically attracted to umbilical points are pushed away, due to repulsive forces between equally charged defects. The competition between these forces determines the equilibrium configuration, which is still free to rotate along the long axis of the ellipsoid [19]. The dynamics follow these equilibrium configurations, with a short delay required to readjust the defect positions, see the solution at $t = 110$. Interestingly, this adjustment also requires to pass the situation where the four $+\frac{1}{2}$ defects are arranged in a planar configuration, see figure 2.

(b) Surface response

Next, we consider stationary Q -tensor fields and investigate the response of the surface to it. In the model (2.13)–(2.14), this can be achieved by using $k^q/k \rightarrow \infty$. Roughly speaking, the time scale of the response of the surface is infinitesimal small compared with the relaxation time scales of the Q -tensor field. We start with the minimal energy configurations on a sphere for the Q -tensor field \mathbf{q} , which was obtained as steady-state solutions of equation (2.14) on the unit sphere with the initial conditions from the prior section. Figure 3 shows the initial condition and the reached steady-state solution after shape relaxation. The shape deviates and becomes asymmetric, see figure 4. The deviation from a sphere is computed according to $\sigma_{S^2} = \int_{S^2} (\mathcal{H} - \mathcal{H}_{S^2})^2 \mu$, where \mathcal{H}_{S^2} denotes the mean curvature of the unit sphere. The relatively small deviation results from the Helfrich-like contribution, cf. (2.13) resulting from the variation of the Landau-de Gennes energy w. r. t. to the surface, which effectively increases bending stiffness and therefore keeps the surface more spherical. The surface is most distorted in the vicinity of the defects, where regions of high Gaussian curvature evolve, see figure 3. A logarithmic scale for Gaussian curvature is used to highlight this.

In figure 4, we approximate shape by a symmetric ellipsoid with the same surface area. The distortions in the vicinity of the defects are visible and the different values for long- and short-axis of the approximating ellipsoids are marked. Figure 4 further highlights the differences of defect positions and points of maximal Gaussian curvature. They are still close to each other but do not coincide. Within the vicinity of the poles on the long axis of the approximating ellipsoids defects and points of maximal curvature are symmetrically arranged on one line, which is rotated by 90°

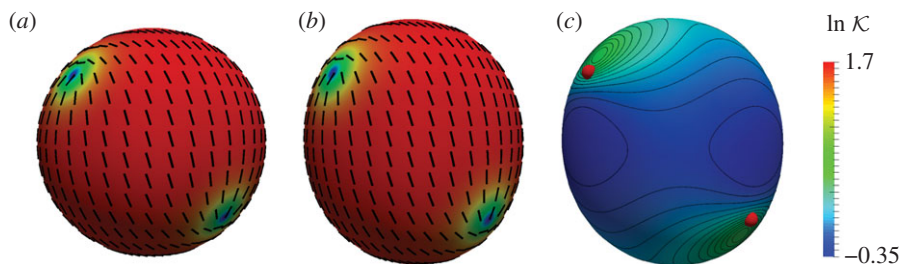


Figure 3. Initial condition for the Landau-de Gennes-Helfrich model as minimal configuration on the sphere (a) and reached steady-state solution (b) with respective Gaussian curvature (c). The contour lines in the Gaussian curvature images indicate constant curvature lines and the red spheres are the positions of the defects. (Online version in colour.)

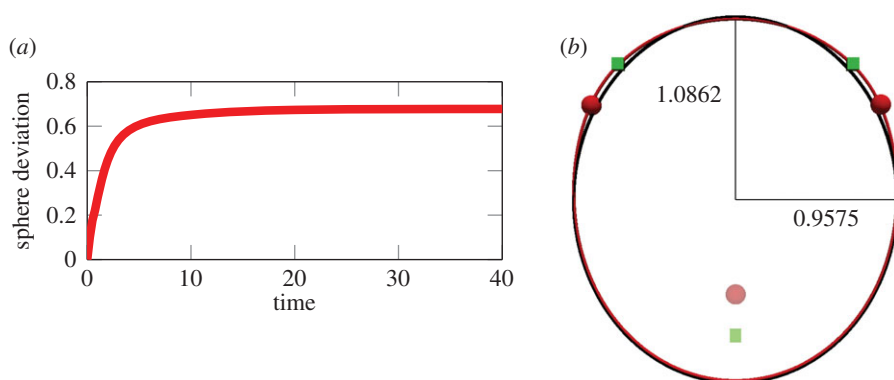


Figure 4. (a) Deviation from a sphere geometry during time evolution. The sphere deviation $\sigma_{\mathcal{S}}$ is considered to be $\sigma_{\mathcal{S}} = \int_{\mathcal{S}} (\mathcal{H} - \mathcal{H}_{\mathcal{S}})^2 \mu$, where $\mathcal{H}_{\mathcal{S}}$ denotes the mean curvature of the unit sphere. (b) Slice of final shape of the Landau-de Gennes-Helfrich model (red), reference is an ellipse (black). The slice is through the upper defect pair. Red spheres are the defect positions (light red sphere indicates the defect pair that does not belong to the slice), green squares are the positions of maximum Gaussian curvature (light green square for corresponding position which does not belong to the slice). Ellipses are fitted such that the surface area corresponds to the surface area of the final shape. (Online version in colour.)

for the two poles. Additional forces which contribute to shape relaxation are due to alignment. In regions of low Gaussian curvature, the director fields are almost perfectly aligned.

(c) Fully coupled system

After investigating either the response of the directors or of the surfaces we now combine both mechanisms by considering the whole system of equations (2.13)–(2.14) in an appropriate parameter setting, cf. table 1. As initial conditions we consider shapes for which Q -tensor fields with more than the minimal number of topologically required defects are energetically favourable. For the polar liquid crystals, this can be considered with a so-called nonic surface [24]. The parametrization of this surface reads

$$X(\theta, \varphi) := X_{S^2}(\theta, \varphi) + f_{C,r}(\cos \theta) \mathbf{e}_x - B \sin \theta \sin \varphi \mathbf{e}_y, \quad (4.1)$$

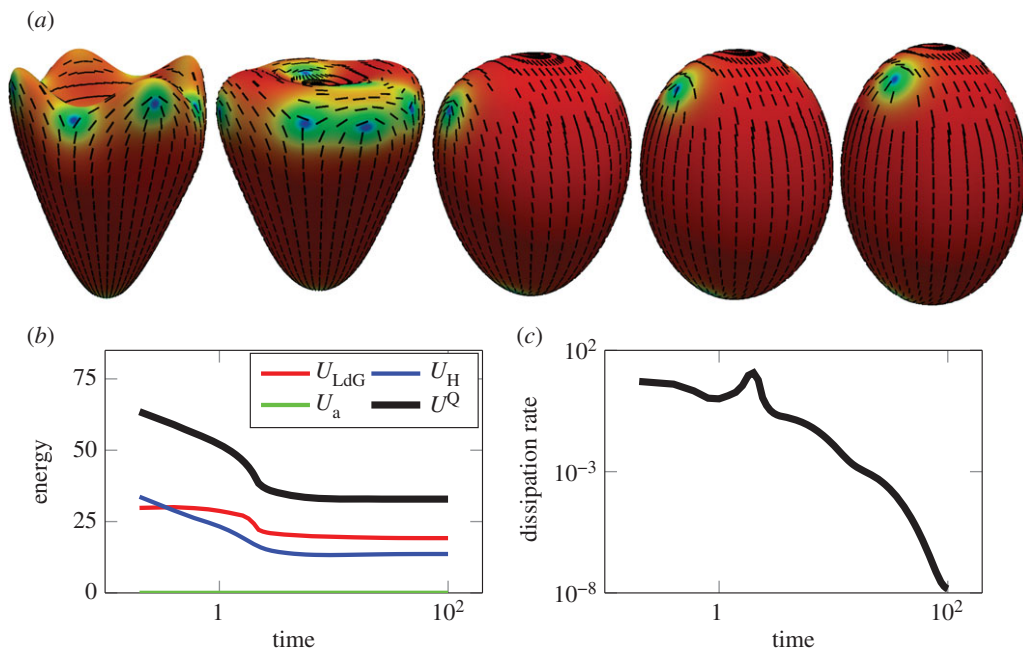


Figure 5. (a) Evolution of the Q -tensor field of the Landau-de Gennes-Helfrich model for $t = 0, 1.5, 5, 10, 100$ for the bi-nonic surface initial condition (left to right). (b) Energies against time (left) and dissipation rate against time (c). See also electronic supplementary material, video.

with standard parametrization angles θ, φ , standard parametrization of the unit sphere $X_{S^2}(\theta, \varphi)$, unit vectors in x, y -direction $\mathbf{e}_x, \mathbf{e}_y$ in \mathbb{R}^3 , parameters $C = 0.75$, $B = \frac{7}{20}C$ and $r = 0.95$ and

$$f_{C,r}(z) := \frac{1}{4}Cz^2 \left((z+1)^2(4-3z) + r(z-1)^2(4+3z) \right).$$

To construct a similar situation for nematic liquid crystals is more complex. A morphology has to be found for which more than four $+\frac{1}{2}$ defects are energetically favourable. We modify the parametrization by using

$$\mathbf{X}(\theta, \varphi) := \mathbf{X}_{S^2}(\theta, \varphi) + f_{C,r}(\cos \theta)\mathbf{e}_x + f_{C,r}(\sin \theta \sin \varphi)\mathbf{e}_y, \quad (4.2)$$

and call this surface bi-nonic. All parameters remain unchanged except of $C = 1.1$. As initial condition we use the steady-state solution on the stationary bi-nonic surface with

$$q|_{t=0} = S \left(\left(\mathbf{v} \times \mathbf{p}_q \right) \otimes \left(\mathbf{v} \times \mathbf{p}_q \right) - \frac{1}{2} \Pi_S \right), \quad \mathbf{p}_q = \frac{1}{\|\Pi_S \mathbf{e}_x\|} \Pi_S \mathbf{e}_x,$$

which consists of eight $+\frac{1}{2}$ defects and four $-\frac{1}{2}$ defects. The positive ones are located in the vicinity of peaks and valleys, while the negative ones can be found around saddle points of the surface. As for the setting for the Frank-Oseen-Helfrich energy in [24], it is demonstrated that this solution is stable and has a lower energy than any configuration with less defects. The geometry, the initial condition and the evolution of both are shown in figure 5. Regions of high curvature become shallower over time such that geometric forces—pushing or pulling defects—become weaker. This results in annihilation of defects (four $\pm\frac{1}{2}$ defect pairs), which can again be observed in the evolution of the energy as well as dissipation rate as step or peak, respectively, cf. figure 5b,c.

Most interesting is the evolution after the annihilation, if only four $+\frac{1}{2}$ defects remain. In contrast to the tetrahedral ground state on a sphere or a rotationally symmetric ellipsoid, here the four $+\frac{1}{2}$ defects arrange in a planar position on a surface which is asymmetric. In figure 6, we show the deviation from a sphere for the Landau-de Gennes-Helfrich model during evolution.

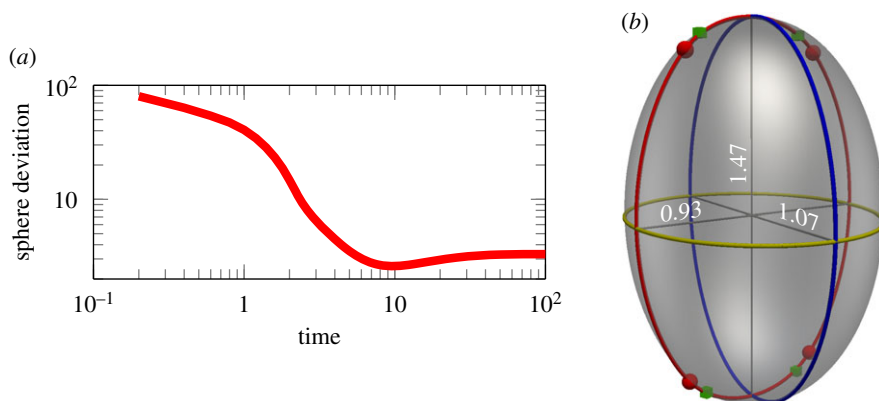


Figure 6. (a) Deviation from a sphere geometry during time evolution. The sphere deviation $\sigma_{\mathcal{S}}$ is considered to be $\sigma_{\mathcal{S}} = \int_{\mathcal{S}} (\mathcal{H} - \mathcal{H}_{\mathcal{S}})^2 \mu$, where $\mathcal{H}_{\mathcal{S}}$ denotes the mean curvature of the unit sphere. (b) Final shape of the Landau-de Gennes-Helfrich model. The values for the axes (distances from the origin) indicate the asymmetry for the nematic case. Red spheres are the defect positions, green squares are the positions of maximum Gaussian curvature. The values correspond to the asymmetric form of the final shape. The defects and points of maximal curvature are located on the same plane (red line). (Online version in colour.)

The increase corresponds with the defect rearrangement and the formation of an asymmetric shape. Defects are visualized as red spheres and the maximal values of the Gaussian curvature are marked as green squares.

The fully coupled system does not only annihilate all topologically unnecessary defects by smoothing the surface it also leads to asymmetric shapes and defect arrangements which differ from ground state configurations on rotationally symmetric ellipsoids.

(d) Discussion

In order to better understand the observed behaviour in the previous section, we run the full model with the equilibrium configuration on an ellipsoid as initial conditions. Figure 7 shows the corresponding evolution together with the energy plot. We observe the same behaviour.

The shape becomes asymmetric and the four $+\frac{1}{2}$ defects arrange in a planar configuration. To observe this behaviour requires long time simulations and an accurate numerical scheme. The energy plot clearly shows that the increase in Helfrich energy \mathcal{U}_H is overcompensated by the decrease in the Landau-de Gennes energy \mathcal{U}_{LDG} . The shape significantly differs from the proposed equilibrium shape in [27], where n -atic order on deformable surfaces is considered, but with a much simpler and purely intrinsic model. More recently, it has been demonstrated that besides these intrinsic curvature terms also extrinsic curvature terms, i. e. curvatures related to the geometry of the embedding space, are relevant [16,18,21,22,24,25,41–47]. It has been demonstrated that the intrinsic geometry tends to confine topological defects to regions of maximal Gaussian curvature, while extrinsic couplings tend to orient the director field along minimal curvature lines. Extrinsic curvature has also been shown to expel defects from regions of maximum curvature above a critical coupling threshold [41], to modify the defect arrangement from tetrahedral to planar [16], to change the phase diagram allowing for coexistence of nematic and isotropic phases in curved two-dimensional liquid crystals [25] and to modify the critical geometry deformation parameter, cf. C , in the considered bi-nonic surface which lead to energetically favourable solutions with more defects than topologically necessary [24]. The observed arrangements thus add to these phenomena and can also be explained by an interplay of intrinsic and extrinsic curvature effects.

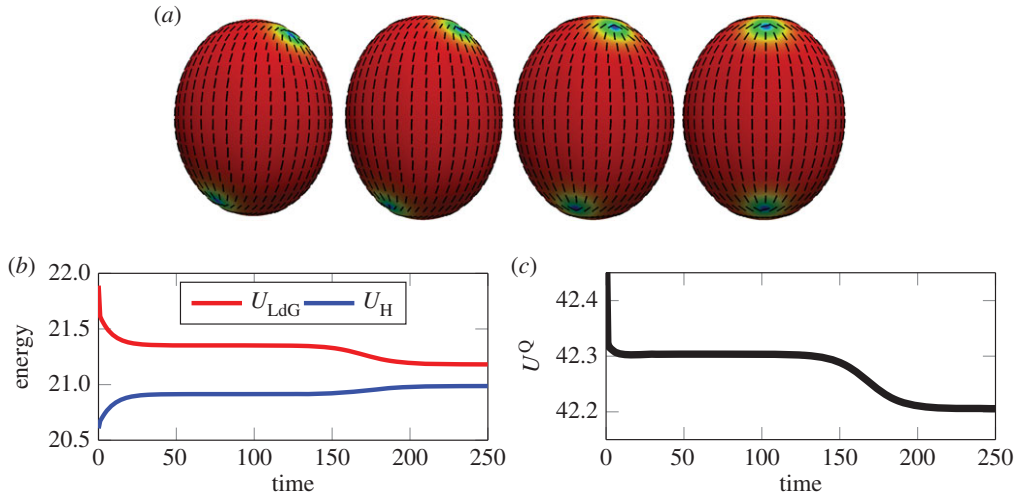


Figure 7. (a) Evolution of the Q -tensor field of the Landau-de Gennes-Helfrich model for $t = 0, 100, 170, 250$. The same initial condition as in figure 1 is used and energy against time (b) and dissipation rates against time (c) are plotted. (Online version in colour.)

Mathematically the extrinsic contributions result from the proposed anchoring conditions on the boundary of the thin film [24,25]. If these terms are neglected the elastic part of the Landau-de Gennes-Helfrich energy has to be modified to

$$\mathcal{U}_{El} = \frac{L}{2} \int_S \|\nabla_S q\|^2 \mu. \quad (4.3)$$

All other energies in equations (2.5)–(2.9) remain. This results in the intrinsic evolution laws for q

$$\begin{aligned} kv = & -\alpha \left(\Delta_S \mathcal{H} + \mathcal{H} \left(\frac{\mathcal{H}^2}{2} - 2\mathcal{K} \right) \right) + \mathcal{H} \left(a' \text{Tr } q^2 + c \text{Tr } q^4 + C_1 \right) \\ & - 2L \text{div}_S (q \nabla_B q - \nabla_B q) - L \left((\nabla_S q)^{T(123)} : \nabla_S q, \Pi_{QS} B \right) + \frac{\omega_a}{A_0^2} (A - A_0) \mathcal{H} \end{aligned} \quad (4.4)$$

and

$$k^q \dot{q} = L \Delta^B q - 2 \left(a' + c \text{Tr } q^2 \right) q. \quad (4.5)$$

This model can be solved with the same numerical approach, just setting various terms to zero. Figure 8 shows the resulting equilibrium shape in comparison with its full model. The equilibrium shape corresponds qualitatively with this in [27]. Defects are located at maximal Gaussian curvature points, the distortion of the surface in the vicinity of the defects is small and a tetrahedral defect arrangement is most favourable for the nematic case. The comparison between the equilibrium shape for the intrinsic and the full model including also extrinsic curvature contributions further highlights the differences.

Our results add to the importance of intrinsic and extrinsic contributions. The derived thermodynamically consistent model for nematic liquid crystals on deformable surfaces and the considered numerical approach to solve these highly nonlinear equations show the tight interplay of these curvature contributions with defect arrangements and shape changes. The results go well beyond purely intrinsic energy minimization approaches. These phenomena do not only change the behaviour quantitatively, they qualitatively lead to new solutions. The symmetric tetrahedral arrangement, which is the basis for proposed self-assembly processes of colloidal particles with tetrahedral structure [7], is not stable if the surface is deformable. We expect these qualitative changes to hold also for more realistic liquid crystal models, beyond the one-constant

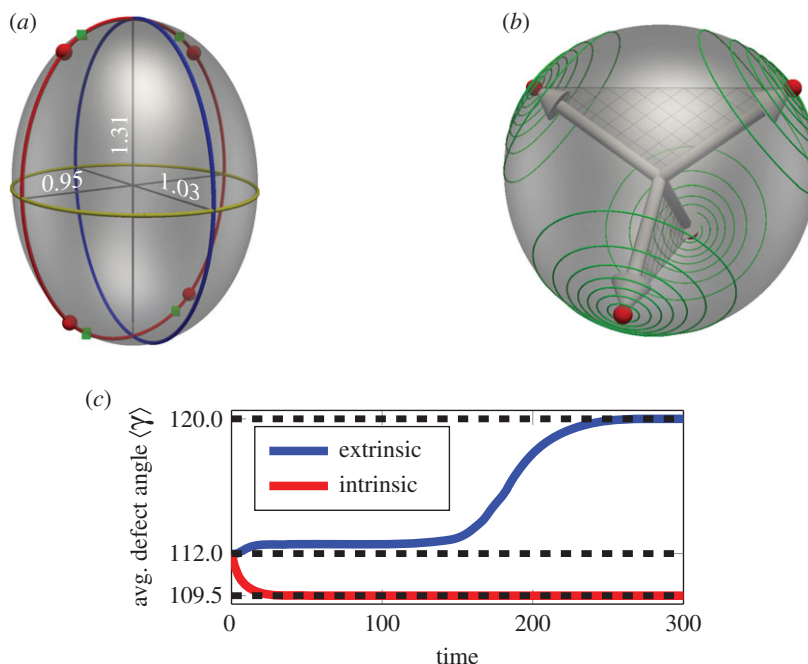


Figure 8. (a) Equilibrium shape obtained with the extrinsic Landau-de Gennes-Helfrich model (2.13), (2.14). Red spheres are the defect positions and green squares are the positions of maximum Gaussian curvature. The distances of the surface from the origin are marked to highlight the asymmetry. All defects and maximal curvature points are located on one plane (red curve). (b) Equilibrium shape obtained with the intrinsic Landau-de Gennes-Helfrich model (4.4), (4.5). The Gaussian curvature is shown as green contour lines. The defect positions correspond with the maximum Gaussian curvature points. They are arranged in a tetrahedral configuration. Initial conditions correspond to figure 7. (c) Averaged defect angle $\langle \gamma \rangle$ (see figure 2) against time for the extrinsic and the intrinsic Landau-de Gennes-Helfrich model; 112° is the equilibrium average for the considered ellipsoid at the initial configuration, 109.5° and 120° correspond to the tetrahedral and planar defect configuration, respectively. (Online version in colour.)

approximation. This will lead to even more curvature coupling terms [25]. The tendency towards asymmetric shapes will even be enhanced, as already present for purely intrinsic models [14]. This will not only influence applications in soft condensed matter based on liquid crystals on flexible curved substrates but also has implications in biophysics, concerning morphological changes during development and the design of bioinspired materials that are capable of self-organization.

Data accessibility. This work does not have any experimental data. Datasets and code are made available at <https://gitlab.mn.tu-dresden.de/sourcecode/surface-lc> [48].

Authors' contributions. I.N. derived the models. S.R. implemented the models and performed finite-element simulations. I.N., S.R. and A.V. conceived and interpreted the numerical experiments. All authors contributed to a critical discussion of the derived model and numerical data and participated in writing the manuscript, which A.V. finalized. A.V. coordinated the project.

Competing interests. We declare we have no competing interests.

Funding. A.V. acknowledges financial support from DFG through Vo899/19 and FOR3013. We further acknowledge computing resources provided by JSC under grant no. HDR06 and ZIH/TU Dresden.

Appendix A

We here provide all necessary details concerning the model and the numerical approach. While an analytical investigation of the model and the numerical approach is beyond the scope of this paper, we thereby restrict ourselves to experimental studies. When convenient, we use

Ricci calculus [49] with lower-case Latin indices. Please note that for ease of terminology we exert parentheses of symmetrizing, e.g. $r_{jl}^{(i\ k)} = \frac{1}{2}(r_{jl}^{ik} + r_{jl}^{ki})$ for a mixed 4-tensor $r \in T_{11}^{11}\mathcal{S}$. To avoid confusion, these parentheses are only used pairwise and always concerning neighbouring indices at the same height of indexing. Another feature concerning the symmetry is that we write one index below the other directly for mixed symmetric 2-tensors, e.g. $B_j^i := B_j^i = B_j^i$, where the latter identity holds, since $B^{ij} = B^{(ij)}$.

Appendix B. Derivations

(a) Shape variations

In the following, we investigate some surface quantities and operators of the surface under perturbation. For consistency with notation of differential geometry, we write $\partial_i := \frac{d}{dy^i}$ for the derivative along local coordinates. This is motivated in the sense that we can use ∂_i as well as partial derivatives, i.e. for a function $f = f(\xi)$ and given ξ we find a function f_ξ such that $f(\xi(t, y^1, y^2), y^1, y^2) = f_\xi(t, y^1, y^2)$ and it holds that $\partial_i f = \partial_i f_\xi = \frac{\partial f_\xi}{\partial y^i}$. Moreover, we observe that the surface variation and ∂_i commute, i.e. $\delta_S \circ \partial_i = \partial_i \circ \delta_S$. For 2-tensor fields $r = r^{ij} \partial_i X \otimes \partial_j X \in T^2\mathcal{S}$ the surface variation δ_S gives

$$\begin{aligned} \Pi_S \delta_S r &= \left(\delta_S r^{ij} \right) \partial_i X \otimes \partial_j X + r^{ij} \Pi_S \left[\partial_i (\delta \xi \mathbf{v}) \otimes \partial_j X + \partial_i X \otimes \partial_j (\delta \xi \mathbf{v}) \right] \\ &= \left(\delta_S r^{ij} \right) \partial_i X \otimes \partial_j X - (B\mathbf{r} + \mathbf{r}B) \delta \xi. \end{aligned} \quad (\text{B } 1)$$

Obviously, symmetric 2-tensor fields are closed under $\Pi_S \delta_S : T^2\mathcal{S} \rightarrow T^2\mathcal{S}$. To show the closeness w. r. t. Q -tensor fields $q \in Q\mathcal{S}$, we observe that $g_{ij} \delta_S q^{ij} = \delta_S \text{Tr } q - q^{ij} \delta_S g_{ij} = 2\langle B, q \rangle \delta \xi$, see equation (B 3) below. Therefore, with equation (B 1) and $\text{Tr} [\partial_i X \otimes \partial_j X] = g_{ij}$ we obtain $\text{Tr } \Pi_S \delta_S q = (\delta_S q^{ij} - [Bq + qB]^{ij}) g_{ij} = 2\langle B, q \rangle \delta \xi - 2\langle B, q \rangle \delta \xi = 0$ and it finally holds

$$\forall q \in Q\mathcal{S} : \Pi_{Q\mathcal{S}} \delta_S q = \left\{ \delta_S q^{ij} \right\} - (Bq + qB) \delta \xi \in Q\mathcal{S}. \quad (\text{B } 2)$$

For the components of the metric tensor, we get

$$\begin{aligned} \delta_S g_{ij} &= \delta_S \langle \partial_i X, \partial_j X \rangle = \langle \partial_i (\delta \xi \mathbf{v}), \partial_j X \rangle + \langle \partial_i X, \partial_j (\delta \xi \mathbf{v}) \rangle = -2 \langle \mathbf{v}, \partial_i \partial_j X \rangle \delta \xi \\ &= -2B_{ij} \delta \xi, \end{aligned} \quad (\text{B } 3)$$

and consequently for the components of the inverse metric tensor

$$\delta_S g^{ij} = 2B^{ij} \delta \xi, \quad (\text{B } 4)$$

which follows from $\delta_S g_{ij} = \delta_S (g_{ik} g_{jl} g^{kl}) = 2\delta_S g_{ij} + g_{ik} g_{jl} \delta_S g^{kl}$ by using the product rule. Using the identity $\mathcal{D} \det g = \det g \text{Tr} \{ \mathcal{D} g_{ij} \}$ for derivatives $\mathcal{D} : T^0\mathcal{S} \rightarrow T^0\mathcal{S}$ acting on scalar-valued functions, we obtain

$$\delta_S \sqrt{\det g} = \frac{1}{2\sqrt{\det g}} \delta_S \det g = \frac{\sqrt{\det g}}{2} \text{Tr} \{ \delta_S g_{ij} \} = -\sqrt{\det g} \mathcal{H} \delta \xi,$$

which finally results in

$$\delta_S \int_{\mathcal{S}} f \mu = \int_{\mathcal{S}} \delta_S f - f \mathcal{H} \delta \xi \mu, \quad (\text{B } 5)$$

for scalar-valued functions f , similar to the well-known transport theorem. Next, we consider the Christoffel symbols which are needed for covariant differentiation. With equation (B 3), the

surface variation of the first kind Christoffel symbols reads

$$\begin{aligned}\delta_S \Gamma_{ijl} &= \frac{1}{2} \delta_S (\partial_i g_{jl} + \partial_j g_{il} - \partial_l g_{ij}) = \frac{1}{2} (\partial_i \delta_S g_{jl} + \partial_j \delta_S g_{il} - \partial_l \delta_S g_{ij}) \\ &= -(\delta \xi_{|i} B_{jl} + \delta \xi_{|j} B_{il} - \delta \xi_{|l} B_{ij}) - \delta \xi (B_{j|l|i} + B_{i|l|j} - B_{ij|l} + 2\Gamma_{ij}^k B_{kl}) \\ &= \delta \xi_{|l} B_{ij} - \delta \xi_{|i} B_{jl} - \delta \xi_{|j} B_{il} - \delta \xi (B_{j|l|i} + 2\Gamma_{ij}^k B_{kl}) \\ &= \delta \xi_{|l} B_{ij} - \delta \xi_{|j} B_{il} - (\delta \xi B_{jl})_{|i} - 2\delta \xi \Gamma_{ij}^k B_{kl},\end{aligned}$$

where we have used that the shape operator is curl-free, i.e. $B_{i|l|j} - B_{ij|l} = 0$. Furthermore, with equation (B 4), it holds for the second kind Christoffel symbols that

$$\delta_S \Gamma_{ij}^k = \delta_S (g^{kl} \Gamma_{ijl}) = 2B^{kl} \Gamma_{ijl} \delta \xi + g^{kl} \delta_S \Gamma_{ijl} = \delta \xi^{lk} B_{ij} - \delta \xi_{|j} B_i^k - (B_i^k \delta \xi)_{|j}.$$

With these evaluations, we obtain for an independent Q -tensor field $q \in \mathcal{QS}$, i.e. $\Pi_{\mathcal{QS}} \delta_S q = 0$ or $\delta_S q^{ij} = [Bq + qB]^{ij} \delta \xi$, respectively, see (B 2), that

$$\begin{aligned}\delta_S q_{|k}^{ij} &= \partial_k \delta_S q^{ij} + 2\Gamma_{kl}^{(i} \delta_S q^{j)l} + 2q^{l(j} \delta_S \Gamma_{kl}^{i)} \\ &= 2(B_l^{(i} q^{j)l} \delta \xi)_{|k} - 2q^{l(j} (B_l^{i)} \delta \xi)_{|k} + \delta \xi_{|l} B_k^{(j} - \delta \xi^{(i} B_{|k}^{j)} \\ &= 2B_l^{(i} q^{j)l} \delta \xi + 2q^{l(j} (\delta \xi^{i)} B_{kl} - \delta \xi_{|l} B_k^{j)})\end{aligned}$$

for the mixed components of $\nabla_S q$. In a fully contravariant sense this reads

$$\delta_S q^{ij|k} = g^{kl} \delta_S q_{|l}^{ij} + q_{|l}^{ij} \delta_S g^{kl} = 2(B_l^{(i} q^{j)l|k} + q^{ij|l} B_l^k) \delta \xi + 2q^{l(j} (\delta \xi^{i)} B_l^k - \delta \xi_{|l} B^{j)k}).$$

In the embedding space, we explicitly obtain

$$\begin{aligned}\Pi_S \delta_S \nabla_S q &= (\delta_S q^{ij|k}) \partial_i X \otimes \partial_j X \otimes \partial_k X \\ &\quad + q^{ij|k} (\partial_i v \otimes \partial_j X \otimes \partial_k X + \partial_i X \otimes \partial_j v \otimes \partial_k X + \partial_i X \otimes \partial_j X \otimes \partial_k v) \delta \xi\end{aligned}$$

for $\nabla_S q = q^{ij|k} \partial_i X \otimes \partial_j X \otimes \partial_k X \in T^3 S$, which finally gives

$$\forall q \in \mathcal{QS} \text{ with } \Pi_{\mathcal{QS}} \delta_S q = 0: [\Pi_S \delta_S \nabla_S q]^{ijk} = B_i^k (q^{ij|l} \delta \xi + 2q^{l(i} \delta \xi^{j)}) - 2B^{k(i} q^{j)l} \delta \xi_{|l}, \quad (\text{B } 6)$$

where $\partial_i v = -B_i^k \partial_k X$ was used.

To determine the behaviour of extrinsic curvature quantities under surface variations, we first consider the normal vector v . The normal part of $\delta_S v$ vanishes and the tangential part is determined by $\langle \delta_S v, \partial_i X \rangle = -\langle v, \partial_i \delta_S X \rangle = -\langle v, \delta \xi \partial_i v + v \partial_i \delta \xi \rangle = -\partial_i \delta \xi$ and thus

$$\delta_S v = -\nabla_S \delta \xi. \quad (\text{B } 7)$$

For the covariant components of the shape operator, we obtain

$$\begin{aligned}\delta_S B_{ij} &= -\delta_S \langle \partial_i X, \partial_j v \rangle = -\langle \partial_i (\delta \xi v), \partial_j v \rangle + \langle \partial_i X, \partial_j \nabla_S \delta \xi \rangle \\ &= -\langle \partial_i v, \partial_j v \rangle \delta \xi + \langle \partial_i X, (\partial_j \delta \xi^{lk}) \partial_k X + \delta \xi^{lk} \partial_j \partial_k X \rangle \\ &= -[B^2]_{ij} \delta \xi + g_{ik} \partial_j \delta \xi^{lk} + \Gamma_{jki} \delta \xi^{lk} = -[B^2]_{ij} \delta \xi + \delta \xi_{|i|j} = [\nabla_S^2 \delta \xi - B^2 \delta \xi]_{ij},\end{aligned}$$

and for the contravariant components

$$\delta_S B^{ij} = [\nabla_S^2 \delta \xi + 3B^2 \delta \xi]^{ij},$$

where $\delta_S B^{ij} = \delta_S (g^{ik} g^{jl} B_{kl})$ and equation (B 4) was used. Furthermore, for the embedded tensor $B = B^{ij} \partial_i X \otimes \partial_j X$, we get

$$\Pi_S \delta_S B = \nabla_S^2 \delta \xi + 3B^2 \delta \xi + B^{ij} (\partial_i v \otimes \partial_j X + \partial_i X \otimes \partial_j v) \delta \xi = \nabla_S^2 \delta \xi + B^2 \delta \xi. \quad (\text{B } 8)$$

Finally, consider the mean curvature \mathcal{H} , for which $\delta_S \mathcal{H} = B_{ij} \delta_S g^{ij} + g^{ij} \delta_S B_{ij}$ can be observed, we obtain

$$\delta_S \mathcal{H} = \Delta_S \delta \xi + \|B\|^2 \delta \xi = \Delta_S \delta \xi + (\mathcal{H}^2 - 2\mathcal{K}) \delta \xi. \quad (\text{B } 9)$$

(b) Functional derivatives

With the tools from above, we are able to compute the functional derivatives of free energies depending on independent scalar field $\xi \in T^0 S$ and Q -tensor field $q \in QS$, i. e. $\Pi_{QS} \delta_S q = 0$. Note that we consider a surface without boundary, which drastically reduces the complexity of the derivations.

(i) Helfrich energy

With equations (B 5) and (B 9), the Helfrich energy \mathcal{U}_H yields, cf. [50, pp. 280–282],

$$\delta_S \mathcal{U}_H = \alpha \int_S \mathcal{H} \delta_S \mathcal{H} - \frac{\mathcal{H}^3}{2} \delta \xi \mu = \alpha \int_S \mathcal{H} \Delta_S \delta \xi + \mathcal{H} \left(\frac{\mathcal{H}^2}{2} - 2\mathcal{K} \right) \delta \xi \mu.$$

Thus, by using integration by parts we get

$$\frac{\delta \mathcal{U}_H}{\delta \xi} = \alpha \left(\Delta_S \mathcal{H} + \mathcal{H} \left(\frac{\mathcal{H}^2}{2} - 2\mathcal{K} \right) \right). \quad (\text{B } 10)$$

(ii) Elastic part of the Landau-de Gennes energy

Consider the elastic part of the Landau-de Gennes energy, i. e. equation (2.6), in the equivalent representation $\mathcal{U}_{\text{El}} = \frac{1}{2} \int_S \|\nabla_S q\|^2 + \langle B^2, r \rangle \mu$, where $r = (\|q\|^2 + \frac{S^2}{2}) \text{Id}_S + 2S q$. Similar to the Frank-Oseen energy above, we call the first summand the intrinsic part and the second one the extrinsic part. Considering the intrinsic part, by equation (B 6) and symmetry arguments, variation of the integrand yields

$$\begin{aligned} \frac{1}{2} \delta_S \|\nabla_S q\|^2 &= \langle \nabla_S q, \Pi_S \delta_S \nabla_S q \rangle = q_{ijkl} \left(B_l^k \left(q^{ijl} \delta \xi + 2q^{li} \delta \xi^{lj} \right) - 2B^{k(i} q^{j)l} \delta \xi_{lj} \right) \\ &= q_{ijkl} \left(B_l^k \left(q^{ijl} \delta \xi + 2q^{li} \delta \xi^{lj} \right) - 2B^{ki} q^{jl} \delta \xi_{lj} \right) \\ &= \left\langle (\nabla_S q)^{T(123)} : \nabla_S q, B \right\rangle \delta \xi + 2 \langle \nabla_q B q - q \nabla_B q, \nabla_S \delta \xi \rangle. \end{aligned}$$

Hence, with equation (B 5), we obtain

$$\begin{aligned} \frac{1}{2} \delta_S \int_S \|\nabla_S q\|^2 \mu &= \frac{1}{2} \int_S \delta_S \|\nabla_S q\|^2 - \left\langle (\nabla_S q)^{T(123)} : \nabla_S q, \text{Id}_S \right\rangle \mathcal{H} \delta \xi \mu \\ &= \int_S \left\langle (\nabla_S q)^{T(123)} : \nabla_S q, \Pi_{QS} B \right\rangle \delta \xi + 2 \langle \nabla_q B q - q \nabla_B q, \nabla_S \delta \xi \rangle \\ &= \int_S \left(\left\langle (\nabla_S q)^{T(123)} : \nabla_S q, \Pi_{QS} B \right\rangle + 2 \text{div}_S [q \nabla_B q - \nabla_q B q] \right) \delta \xi \mu. \end{aligned}$$

For the extrinsic part, we observe that the 2-tensor $r \in T^2 S$ is also a surface independent tensor quantity, i. e. $\Pi_S \delta_S r = 0$, as $\Pi_S \delta_S q = 0$ and $\Pi_S \delta_S \text{Id}_S = \Pi_S \delta_S (g^{ij} \partial_i X \otimes \partial_j X) = 0$. Therefore, by using the product rule, the symmetric behaviours and equation (B 8), we obtain $\frac{1}{2} \delta_S \langle B^2, r \rangle = \langle B \delta_S B, r \rangle = \langle r B, \delta_S B \rangle = \langle r B, \nabla_S^2 \delta \xi + B^2 \delta \xi \rangle = \langle r B, \nabla_S^2 \delta \xi \rangle + (\mathcal{H}^2 - \mathcal{K}) \langle r, B \rangle \delta \xi - \mathcal{H} \mathcal{K} \text{Tr } r \delta \xi$, where we

have used $B^3 = (\mathcal{H}^2 - \mathcal{K})B - \mathcal{H}\mathcal{K} \text{Id}_S$. Furthermore, with equation (B 5) and $B^2 = \mathcal{H}B - \mathcal{K} \text{Id}_S$, this results in

$$\begin{aligned} \frac{1}{2} \delta_S \int_S \langle B^2, r \rangle \mu &= \frac{1}{2} \int_S \delta_S \langle B^2, r \rangle - \mathcal{H}^2 \langle r, B \rangle \delta \xi + \mathcal{H}\mathcal{K} \text{Tr } r \delta \xi \mu \\ &= \int_S \left(\text{div}_S \text{div}_{S,2} (rB) + \left(\frac{\mathcal{H}^2}{2} - \mathcal{K} \right) \langle B, r \rangle - \frac{\mathcal{H}\mathcal{K}}{2} \text{Tr } r \right) \delta \xi \mu \\ &= \int_S \left(\text{div}_S (\nabla_B r + r \nabla_S \mathcal{H}) + \left(\frac{\mathcal{H}^2}{2} - \mathcal{K} \right) \langle B, r \rangle - \frac{\mathcal{H}\mathcal{K}}{2} \text{Tr } r \right) \delta \xi \mu. \end{aligned} \quad (\text{B } 11)$$

Next, we reinsert $r = (\|q\|^2 + \frac{S^2}{2}) \text{Id}_S + 2Sq$ term by term, i. e.

$$\begin{aligned} [\nabla_B r]_i &= B^{kl} \left[\left(q^{mn} q_{mn} + \frac{S^2}{2} \right) g_{ik} + 2Sq_{ik} \right]_{|l} = 2B^{kl} (q^{mn} q_{mn|l} g_{ik} + Sq_{ik|l}) \\ &= 2[q : (\nabla_S q)B + S\nabla_B q]_i \\ r \nabla_S \mathcal{H} &= \left(\text{Tr } q^2 + \frac{S^2}{2} \right) \nabla_S \mathcal{H} + 2Sq \nabla_S \mathcal{H} \\ \langle B, r \rangle &= \left(\text{Tr } q^2 + \frac{S^2}{2} \right) \mathcal{H} + 2S \langle B, q \rangle \\ \text{Tr } r &= 2\text{Tr } q^2 + S^2. \end{aligned}$$

Therefore, equation (B 11) results in

$$\begin{aligned} \frac{1}{2} \delta_S \int_S \langle B^2, r \rangle \mu &= \int_S \left(2 \text{div}_S \left(q : (\nabla_S q)B + S\nabla_B q + \frac{1}{2} \text{Tr } q^2 \nabla_S \mathcal{H} + Sq \nabla_S \mathcal{H} \right) \right. \\ &\quad \left. + \frac{S^2}{2} \Delta_S \mathcal{H} + S \|B\|^2 \langle B, q \rangle + \mathcal{H} \left(\frac{\mathcal{H}^2}{2} - 2\mathcal{K} \right) \left(\text{Tr } q^2 + \frac{S^2}{2} \right) \right) \delta \xi \mu. \end{aligned}$$

Finally, we sum up the results for the intrinsic and extrinsic parts and get

$$\begin{aligned} \frac{\delta \mathcal{U}_{\text{EI}}}{\delta \xi} &= L \left[2 \text{div}_S \left(q \nabla_B q - \nabla_B q + q : (\nabla_S q)B + S\nabla_B q + \frac{1}{2} \text{Tr } q^2 \nabla_S \mathcal{H} + Sq \nabla_S \mathcal{H} \right) \right. \\ &\quad \left. + S \|B\|^2 \langle B, q \rangle + \mathcal{H} \left(\frac{\mathcal{H}^2}{2} - 2\mathcal{K} \right) \text{Tr } q^2 + \left((\nabla_S q)^{T(123)} : \nabla_S q, \Pi_{QS} B \right) \right. \\ &\quad \left. + \frac{S^2}{2} \left(\Delta_S \mathcal{H} + \mathcal{H} \left(\frac{\mathcal{H}^2}{2} - 2\mathcal{K} \right) \right) \right] \\ \frac{\delta \mathcal{U}_{\text{EI}}}{\delta q} &= L \left[-\mathbf{A}^B q + \|B\|^2 q + S\mathcal{H} \Pi_{QS} B \right]. \end{aligned}$$

(iii) Bulk energy part of the Landau-de Gennes energy

For the bulk energy part of the Landau-de Gennes energy \mathcal{U}_B , by using $\delta_S \text{Tr } q^2 = 2\langle q, \delta_S q \rangle = 0$ and $\delta_S \text{Tr } q^4 = \text{Tr } q^2 \delta_S \text{Tr } q^2 = 0$ it can be easily seen that the energy density is independent w. r. t. perturbation. Hence, equation (B 5) yields

$$\delta_S \mathcal{U}_B = - \int_S \mathcal{H} (a' \text{Tr } q^2 + c \text{Tr } q^4 + C_1) \delta \xi \mu,$$

and therefore

$$\frac{\delta \mathcal{U}_B}{\delta \xi} = -\mathcal{H} (a' \text{Tr } q^2 + c \text{Tr } q^4 + C_1), \quad \frac{\delta \mathcal{U}_B}{\delta q} = 2 (a' + c \text{Tr } q^2) q.$$

(iv) Surface area penalization energy

Considering equation (B5) and the surface area penalization energy \mathcal{U}_a with $A := \int_S \mu$, it follows that

$$\delta_S \mathcal{U}_a = \frac{\omega_a}{A_0^2} (A - A_0) \delta_S A = -\frac{\omega_a}{A_0^2} (A - A_0) \int_S \mathcal{H} \delta \xi \mu.$$

Thus, the functional derivative of the penalization energy is given by

$$\frac{\delta \mathcal{U}_a}{\delta \xi} = -\frac{\omega_a}{A_0^2} (A - A_0) \mathcal{H}.$$

Appendix C. Operators

The contravariant components of some of the used operators are considered, i.e. $[\Delta^B q]^{ij} = q_{|k}^{ij|k}$, $[q \nabla_B q]^i = q^{ij} B^{kl} q_{jk|l}$, $[\nabla_q B q]^i = q_{jk} B^{kl} q_{|l}^{ij}$, $[q : (\nabla_S q) B]^i = q^{jk} B^{li} q_{jk|l}$, $[\nabla_B q]^i = B_{jk} q^{ij|k}$ and $[(\nabla_S q)^{T(123)} : \nabla_S q]^{ij} = q^{kl|i} q_{kl}^{ij}$.

Appendix D. Kinetic considerations

We consider kinetic properties, i.e. time-dependent behaviours of some quantities such as material time derivative, rate of normal vector or energy dissipation.

(a) Time derivative

Since particle motion is considered only in The normal direction, the Lagrangian and the transversal or intrinsic Eulerian observer coincide due to vanishing relative velocity. For simplicity, we here only consider these equivalent observers and define the material time derivative covariantly by the tangential part of the time derivative in the embedding space and denote it by a dot. Thus, for scalar fields $f \in T^0 S$, vector fields $p \in T^1 S$ and 2-tensor fields $r \in T^2 S$ we state that

$$\dot{f} := \partial_t f \quad (D1)$$

$$\dot{p} := \Pi_S [\partial_t p] = g^{ik} \langle \partial_t p, \partial_k X \rangle \partial_i X \quad (D2)$$

$$\text{and} \quad \dot{r} := \Pi_S [\partial_t r] = g^{ik} g^{jl} \langle \partial_t r, \partial_k X \otimes \partial_l X \rangle \partial_i X \otimes \partial_j X. \quad (D3)$$

With chain rule, $v \perp \partial_k X$ and (2.1) the covariant components of \dot{p} read

$$[\dot{p}]_k = \langle \partial_t p, \partial_k X \rangle = \langle (\partial_t p^i) \partial_i X + p^i \partial_i \dot{X}, \partial_k X \rangle = g_{ik} \partial_t p^i - v p^i B_{ik}, \quad (D4)$$

which eventually gives the time derivative of the vector field p in terms of contravariant proxy rates, i.e.

$$\dot{p} = (\partial_t p^i) \partial_i X - v B p. \quad (D5)$$

Analogously, we obtain for the 2-tensor field r that

$$\dot{r} = (\partial_t r^{ij}) \partial_i X \otimes \partial_j X - v (B r + r B). \quad (D6)$$

Similar to the surface variation δ_S , the time derivative for 2-tensors is closed w. r. t. symmetry and trace-free behaviour. This means, it holds for all $q \in QS$ that $\dot{q} \in QS$, since $\partial_t g_{ij} = -2v B_{ij}$ and thus $g_{ij} \partial_t q^{ij} = 2v \langle B, q \rangle$.

(b) Normal vector rate

Equation (2.1), $\mathbf{v} \perp \partial_i \mathbf{X}$ and $\|\mathbf{v}\| = 1$ yield

$$\begin{aligned} \partial_t \mathbf{v} &= \langle \partial_t \mathbf{v}, \mathbf{v} \rangle \mathbf{v} + g^{ij} \langle \partial_t \mathbf{v}, \partial_j \mathbf{X} \rangle \partial_i \mathbf{X} = -g^{ij} \langle \mathbf{v}, \partial_j \dot{\mathbf{X}} \rangle \partial_i \mathbf{X} = -g^{ij} \langle \mathbf{v}, (\partial_j v) \mathbf{v} \rangle \partial_i \mathbf{X} \\ &= -\nabla_S v. \end{aligned} \quad (\text{D } 7)$$

A similar evolving geometric quantity has been considered in [51] in the context of mean curvature flow.

(c) Dissipation of energy

With the L^2 -gradient flow (2.13)–(2.14), the assumption of independence and the theorem below the energy dissipation rate is given by

$$\frac{d}{dt} \mathcal{U}^Q = - \left(k \|\mathbf{v}\|_{L^2(S, T^0 S)}^2 + k^q \|\dot{\mathbf{q}}\|_{L^2(S, \mathcal{Q} S)}^2 \right) \leq 0, \quad (\text{D } 8)$$

i.e. the energy decrease in a L^2 -manner, similar to classical geometric evolution equations of L^2 -gradient flows structure and L^2 -gradient flows on stationary surfaces, as considered in [25].

Theorem D.1. Assume that a tensor field $\mathbf{r} \in T^n S$ is independent of a surface $S = S[\xi]$ in the sense of $\Pi_S \delta_S \mathbf{r} = 0$ or $\frac{d\mathbf{r}}{d\xi} = 0$, equivalently. Then it holds for an energy functional $\mathcal{U} = \mathcal{U}[\xi, \mathbf{r}]$ the chain rule

$$\frac{d}{dt} \mathcal{U} = \nabla_{(\dot{\xi}, \dot{\mathbf{r}})}^* \mathcal{U} := \left(\frac{\delta \mathcal{U}}{\delta \xi} \right)^* [\dot{\xi}] + \left(\frac{\delta \mathcal{U}}{\delta \mathbf{r}} \right)^* [\dot{\mathbf{r}}], \quad (\text{D } 9)$$

where the star $*$ denotes the dual element w. r. t. the L^2 -inner product.

Proof. By linearity of the integral, it is sufficient to show this statement on a subset $\Sigma := X[\xi](Y) \subseteq S$ with $Y = (y^1, y^2) \subset \mathbb{R}^2$. To use common differential calculus locally, we formulate the energy functional as

$$\mathcal{U}_\Sigma[\xi, \mathbf{r}] = \int_\Sigma u(\xi, \mathbf{r}) \mu = \int_Y f(\xi, \mathbf{r}) dY,$$

where $dY = dy^1 \wedge dy^2$, i.e. the function f equals energy density u times area density function $\sqrt{\det g} = \sqrt{\det g(\xi)}$. By definitions of functional and function derivative and the independence between ξ and \mathbf{r} the right-hand side of (D 9) reads

$$\begin{aligned} \nabla_{(\dot{\xi}, \dot{\mathbf{r}})}^* \mathcal{U}_\Sigma &= \lim_{\epsilon_\xi \rightarrow 0} \frac{\mathcal{U}_\Sigma[\xi + \epsilon_\xi \dot{\xi}, \mathbf{r}] - \mathcal{U}_\Sigma[\xi, \mathbf{r}]}{\epsilon_\xi} + \lim_{\epsilon_r \rightarrow 0} \frac{\mathcal{U}_\Sigma[\xi, \mathbf{r} + \epsilon_r \dot{\mathbf{r}}] - \mathcal{U}_\Sigma[\xi, \mathbf{r}]}{\epsilon_r} \\ &= \int_Y \lim_{\epsilon_\xi \rightarrow 0} \frac{f(\xi + \epsilon_\xi \dot{\xi}, \mathbf{r}) - f(\xi, \mathbf{r})}{\epsilon_\xi} + \lim_{\epsilon_r \rightarrow 0} \frac{f(\xi, \mathbf{r} + \epsilon_r \dot{\mathbf{r}}) - f(\xi, \mathbf{r})}{\epsilon_r} dY \\ &= \int_Y \left(\frac{\partial f}{\partial \xi} \right) \dot{\xi} + \left(\frac{\partial f}{\partial \mathbf{r}} \right)^* (\dot{\mathbf{r}}) dY = \int_Y \left(\frac{df}{d\xi} \right) \frac{d\xi}{dt} + \left\langle \frac{df}{d\mathbf{r}}, \frac{d\mathbf{r}}{dt} \right\rangle_{\mathbb{R}^3} dY \\ &= \int_Y \frac{d}{dt} f dY = \frac{d}{dt} \mathcal{U}_\Sigma, \end{aligned}$$

since $df/d\mathbf{r} \in T^n S$.

Actually, the circuit over the local \mathbb{R}^3 -inner product is not necessary, if we reformulate f such that it depends on the contravariant proxy functions of the tensor field \mathbf{r} , partially. To sum up, we have

$$\left(\frac{d\tilde{f}}{d\xi} \right) \dot{\xi} + \left(\frac{d\tilde{f}}{d\mathbf{p}} \right)^* (\dot{\mathbf{p}}) = \frac{\partial \tilde{f}}{\partial \xi} \frac{d\xi}{dt} + \frac{\partial \tilde{f}}{\partial p^i} \frac{dp^i}{dt} = \frac{d}{dt} \tilde{f} = \frac{d}{dt} f.$$

Note that for $n > 1$ the argumentation would be exactly the same, but with 2^n contravariant proxy functions. For $n = 0$, the situation is much simpler, since $\tilde{f} = f$. Note that in this case the projection Π_S stated in the assumption is just the scalar identity. ■

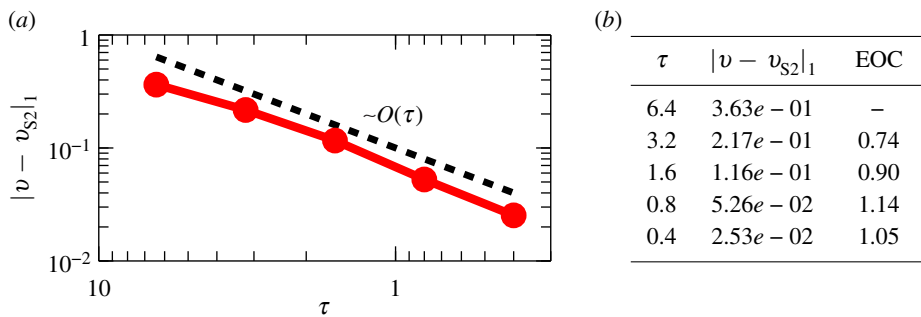


Figure 9. (a) Normal vector error against time-step width τ . Thereby, $|\cdot|_1$ denotes the spatial H^1 semi-norm and v_{S^2} is the normal vector of the unit sphere. (b) Normal vector error together with experimental order of convergence (EOC) values for various time-step widths τ . (Online version in colour.)

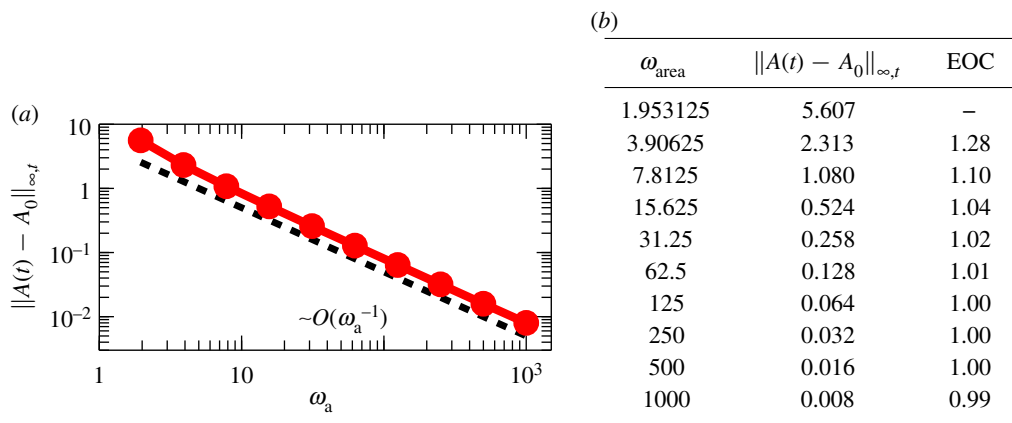


Figure 10. (a) Initial condition as stable configuration on the unit sphere (top left), reached steady-state solution on the deformed surface (top right) and surface area error against surface area penalization parameter ω_a (bottom) with the temporal maximum norm $\|\cdot\|_{\infty,t}$. (b) Surface area error together with experimental order of convergence (EOC) values for various surface area penalization parameters ω_a . (Online version in colour.)

Appendix E. Numerical tests

(a) Numerical computation of geometric quantities

To numerically solve equation (2.13) requires a *sound approximation* of all geometric quantities. They all can be computed from the normal vector, which is obtained through $\partial_t v = -\nabla_S v$, see equation (D7). This approach turns out to be much more accurate than the often used (weighted) element normal vector. We show the numerical convergence (by means of the time-step width τ) of this equation for the Helfrich and the surface area penalization energy for an ellipsoidal shape with axes parameters (1, 1, 1.25) as initial geometry. The ellipsoid converges to a sphere, for which the normal vector is analytically known. Thus, we compare the computed normal vector according to equation (D7) and the analytical one in the steady-state regime according to the H^1 semi-norm. Figure 9 shows the results, where a linear convergence rate w. r. t. the time-step width τ can be observed. It is noted that we use a much smaller time-step width—according to table 1—for the simulation as for the convergence evaluations in figure 9 in order to reduce the temporal error made in the normal velocity equation.

(b) Surface area conservation

In the Landau-de Gennes-Helfrich model, the surface area penalization energy is included in order to achieve constant surface area over time. This approximation depends on the penalty parameter ω_a . In the following, the convergence rate w. r. t. ω_a is numerically investigated. Here, we use qualitatively the same setup as in Figure 3, but with slightly different parameters, see table 1. The results are shown in figure 10, where a linear convergence rate w. r. t. ω_a can be observed.

References

1. Bowick MJ, Giomi L. 2009 Two-dimensional matter: order, curvature and defects. *Adv. Phys.* **58**, 449–563. (doi:10.1080/00018730903043166)
2. Serra F. 2016 Curvature and defects in nematic liquid crystals. *Liq. Cryst.* **43**, 1920–1936. (doi:10.1080/02678292.2016.1209698)
3. Bausch A, Bowick M, Cacciuto A, Dinsmore A, Hsu M, Nelson D, Nikolaides M, Travesset A, Weitz D. 2003 Grain boundary scars and spherical crystallography. *Science* **299**, 1716–1718. (doi:10.1126/science.1081160)
4. Irvine WTM, Vitelli V, Chaikin PM. 2010 Pleats in crystals on curved surfaces. *Nature* **468**, 947–951. (doi:10.1038/nature09620)
5. Jesenek D, Kralj S, Rosso R, Virga EG. 2015 Defect unbinding on a toroidal nematic shell. *Soft Matter* **11**, 2434–2444. (doi:10.1039/C4SM02540G)
6. Lubensky T, Prost J. 1992 Orientational order and vesicle shape. *J. Phys. II* **2**, 371–382. (doi:10.1051/jp2:1992133)
7. Nelson D. 2002 Toward a tetravalent chemistry of colloids. *Nano Lett.* **2**, 1125–1129. (doi:10.1021/nl0202096)
8. Seung H, Nelson D. 1988 Defects in flexible membranes with crystalline order. *Phys. Rev. A* **38**, 1005–1018. (doi:10.1103/PhysRevA.38.1005)
9. Lidmar J, Mirny L, Nelson D. 2003 Virus shapes and buckling transitions in spherical shells. *Phys. Rev. E* **68**, 051910. (doi:10.1103/PhysRevE.68.051910)
10. Aland S, Raetz A, Roeger M, Voigt A. 2012 Buckling instability of viral capsids - a continuum approach. *Multisc. Model. Sim.* **10**, 82–110. (doi:10.1137/110834718)
11. Nelson D. 1983 Order, frustration, and defects in liquids and glasses. *Phys. Rev. B* **28**, 5515–5535. (doi:10.1103/PhysRevB.28.5515)
12. Dzubielia J, Schmidt M, Lowen H. 2000 Topological defects in nematic droplets of hard spherocylinders. *Phys. Rev. E* **62**, 5081–5091. (doi:10.1103/PhysRevE.62.5081)
13. Bates MA, Skacej G, Zannoni C. 2010 Defects and ordering in nematic coatings on uniaxial and biaxial colloids. *Soft Matter* **6**, 655–663. (doi:10.1039/B917180K)
14. Shin H, Bowick MJ, Xing X. 2008 Topological defects in spherical nematics. *Phys. Rev. Lett.* **101**, 037802. (doi:10.1103/PhysRevLett.101.037802)
15. Prinsen P, van der Schoot P. 2003 Shape and director-field transformation of tactoids. *Phys. Rev. E* **68**, 021701. (doi:10.1103/PhysRevE.68.021701)
16. Nguyen TS, Geng J, Selinger RLB, Selinger JV. 2013 Nematic order on a deformable vesicle: theory and simulation. *Soft Matter* **9**, 8314–8326. (doi:10.1039/c3sm50489a)
17. Martínez A, Ravník M, Lucero B, Visvanathan R, Zumer S, Smalyukh II. 2014 Mutually tangled colloidal knots and induced defect loops in nematic fields. *Nat. Mater.* **13**, 259–264. (doi:10.1038/nmat3840)
18. Segatti A, Snarski M, Veneroni M. 2014 Equilibrium configurations of nematic liquid crystals on a torus. *Phys. Rev. E* **90**, 012501. (doi:10.1103/PhysRevE.90.012501)
19. Alaimo F, Koehler C, Voigt A. 2017 Curvature controlled defect dynamics in topological active nematics. *Sci. Rep.* **7**, 5211. (doi:10.1038/s41598-017-05612-6)
20. Kralj S, Rosso R, Virga EG. 2011 Curvature control of valence on nematic shells. *Soft Matter* **7**, 670–683. (doi:10.1039/C0SM00378F)
21. Napoli G, Vergori L. 2012a Surface free energies for nematic shells. *Phys. Rev. E* **85**, 061701. (doi:10.1103/PhysRevE.85.061701)
22. Napoli G, Vergori L. 2012b Extrinsic curvature effects on nematic shells. *Phys. Rev. Lett.* **108**, 207803. (doi:10.1103/PhysRevLett.108.207803)

23. Golovaty D, Alberto Montero J, Sternberg P. 2017 Dimension reduction for the Landau-de Gennes model on curved nematic thin films. *J. Nonlin. Sci.* **27**, 1905–1932. (doi:10.1007/s00332-017-9390-5)
24. Nestler M, Nitschke I, Praetorius S, Voigt A. 2018 Orientational order on surfaces: the coupling of topology, geometry, and dynamics. *J. Nonlin. Sci.* **28**, 147–191. (doi:10.1007/s00332-017-9405-2)
25. Nitschke I, Nestler M, Praetorius S, Löwen H, Voigt A. 2018 Nematic liquid crystals on curved surfaces—a thin film limit. *Proc. R. Soc. A* **474**, 20170686. (doi:10.1098/rspa.2017.0686)
26. Nitschke I, Reuther S, Voigt A. 2019 Hydrodynamic interactions in polar liquid crystals on evolving surfaces. *Phys. Rev. Fluids* **4**, 044002. (doi:10.1103/PhysRevFluids.4.044002)
27. Park J, Lubensky T, MacKintosh F. 1992 N-atic order and continuous shape changes of deformable surfaces of genus zero. *Europhys. Lett.* **20**, 279–284. (doi:10.1209/0295-5075/20/3/015)
28. Keber FC, Loiseau E, Sanchez T, DeCamp SJ, Giomi L, Bowick MJ, Marchetti MC, Dogic Z, Bausch AR. 2014 Topology and dynamics of active nematic vesicles. *Science* **345**, 1135–1139. (doi:10.1126/science.1254784)
29. Marsden J, Hughes T. 2012 *Mathematical foundations of elasticity*. Dover Civil and Mechanical Engineering. Dover Publications.
30. Nestler M, Nitschke I, Voigt A. 2019 A finite element approach for vector- and tensor-valued surface PDEs. *J. Comput. Phys.* **389**, 48–61. (doi:10.1016/j.jcp.2019.03.006)
31. Reuther S, Voigt A. 2018 Solving the incompressible surface Navier-Stokes equation by surface finite elements. *Phys. Fluids* **30**, 012107. (doi:10.1063/1.5005142)
32. Vey S, Voigt A. 2007 AMDiS: adaptive multidimensional simulations. *Comput. Vis. Sci.* **10**, 57–67. (doi:10.1007/s00791-006-0048-3)
33. Witkowski T, Ling S, Praetorius S, Voigt A. 2015 Software concepts and numerical algorithms for a scalable adaptive parallel finite element method. *Adv. Comput. Math.* **41**, 1145–1177. (doi:10.1007/s10444-015-9405-4)
34. Dziuk G, Elliott CM. 2013 Finite element methods for surface PDEs. *Acta Numer.* **22**, 289–396. (doi:10.1017/S0962492913000056)
35. Smereka P. 2003 Semi-implicit level set methods for curvature and surface diffusion motion. *J. Sci. Comput.* **19**, 439–456. (doi:10.1023/A:1025324613450)
36. Rusu R. 2005 An algorithm for the elastic flow of surfaces. *Inerf. Free Boundaries* **7**, 229–239. (doi:10.4171/IFB/122)
37. Barrett J, Garcke H, Nuernberg R. 2007 Parametric approximation of Willmore flow and related geometric evolution equations. *SIAM J. Sci. Comput.* **31**, 225–253. (doi:10.1137/070700231)
38. Dziuk G. 2008 Computational parametric Willmore flow. *Numer. Math.* **111**, 55–80. (doi:10.1007/s00211-008-0179-1)
39. Kovacs B, Li B, Lubich C. 2019 A convergent evolving finite element algorithm for mean curvature flow of closed surfaces. *Numer. Math.* **43**, 797–853. (doi:10.1007/s00211-019-01074-2)
40. Oza AU, Dunkel J. 2016 Antipolar ordering of topological defects in active liquid crystals. *New J. Phys.* **18**, 093006. (doi:10.1088/1367-2630/18/9/093006)
41. Mbanda BL, Grason GM, Santangelo CD. 2012 Frustrated order on extrinsic geometries. *Phys. Rev. Lett.* **108**, 017801. (doi:10.1103/PhysRevLett.108.017801)
42. Napoli G, Vergori L. 2016 Hydrodynamic theory for nematic shells: the interplay among curvature, flow, and alignment. *Phys. Rev. E* **94**, 020701. (doi:10.1103/PhysRevE.94.020701)
43. Segatti A, Snarski M, Veneroni M. 2016 Analysis of a variational model for nematic shells. *Math. Mod. Methods Appl. Sci.* **26**, 1865–1918. (doi:10.1142/S0218202516500470)
44. Koning V, Lopez-Leon T, Darmon A, Fernandez-Nieves A, Vitelli V. 2016 Spherical nematic shells with a threefold valence. *Phys. Rev. E* **94**, 012703. (doi:10.1103/PhysRevE.94.012703)
45. Duan X, Yao Z. 2017 Curvature-driven stability of defects in nematic textures over spherical disks. *Phys. Rev. E* **95**, 062706. (doi:10.1103/PhysRevE.95.062706)
46. Napoli G, Vergori L. 2018 Influence of the extrinsic curvature on two-dimensional nematic films. *Phys. Rev. E* **97**, 052705. (doi:10.1103/PhysRevE.97.052705)

47. Nitschke I, Reuther S, Löwen H, Voigt A. 2020 Properties of surface Landau-de Gennes Q-tensor models. *Soft Matter* **16**, 4032–4042. (doi:10.1039/C9SM02475A)
48. Nitschke I, Reuther S, Voigt A. 2019 Data from: Liquid crystals on deformable surfaces. See <https://gitlab.mn.tu-dresden.de/sourcecode/surface-lc>.
49. Schouten J. 1954 *Ricci-calculus: an introduction to tensor analysis and its geometrical applications*. Die Grundlehren der mathematischen Wissenschaften in Einzeldarstellungen. Springer.
50. Willmore T. 1996 *Riemannian Geometry*. Oxford science publications. Clarendon Press.
51. Huisken G. 1984 Flow by mean curvature of convex surfaces into spheres. *J. Diff. Geometry* **20**, 237–266. (doi:10.4310/jdg/1214438998)